NEUTRAL PION PRODUCTION IN pp AND dAu COLLISIONS AT RHIC

by

ALEXANDER STOLPOVSKY

PROSPECTUS

Submitted to the Graduate School

of Wayne State University,

Detroit, Michigan

in partial fulfillment of the requirements

for the degree of

DOCTOR OF PHILOSOPHY

2004

MAJOR: NUCLEAR PHYSICS

Approved by:

_____

Advisor Date

_____

_____

_____

Contents

List of Figures

Chapter 1

Introduction

Heavy ion collisions at relativistic energies enable scientists to test nuclear matter at high temperature and density and to produce conditions similar to those thought prevalent in the early universe.

Matter is made of leptons, quarks and force mediators. Quarks carry *color*, a property similar to electric charge. The theory that describes the forces between colored objects and is thought to be the correct theory of strong interaction is called quantum chromodynamics (QCD). In QCD, just as the electromagnetic force is carried by photons, the color force (or strong force) is carried by gluons. Unlike photons that are electrically neutral, gluons carry color charge so they can interact directly with each other. Strong coupling constant α_s can be larger than unity. Due to direct gluon-gluon coupling the *effective* strong coupling constant becomes small at short distances, the effect known as *asymptotic freedom*. The force between quarks is stronger at larger distances so quarks are confined to a small ($1fm^3$) region in colorless groups of two (mesons) or three (baryons). Perturbation theory can be used with QCD only when the effective coupling constant is small, a regime achieved in reactions involving large momentum transfers (*hard processes*).

Perturbative QCD (pQCD) is in very good agreement with experimental data from hard processes. However it fails to describe processes that dominate universe at present: soft processes.

To understand the behavior of colored objects where pQCD is not a valid approximation, physicists rely on numerical path integrals of the QCD Lagrangian on a discretized lattice in four-dimensional Euclidian space-time. Lattice QCD can be used to perform numerical calculations for all physics regimes. However there are regimes where approximations used to simplify the calculations fail and computations become technically extremely challenging.

Deconfined quarks have never been observed because the force between colored objects increases linearly with the distance between them. A deconfined quark is one that can move in a volume much larger than that of a proton. QCD predicts that at sufficiently large temperature and density a regime can be reached where quarks and gluons become deconfined.

The new state of matter where quarks and gluons are deconfined, was postulated to exist within the cores of neutron stars [1]. A neutron has a density of about $1 \times 10^{14}\ g/cm^3$, whereas the density in the center of a neutron star can be as much as 10^{16} – $10^{17}\ g/cm^3$. In this case hadrons overlap and the nuclear matter becomes a quark-gluon plasma or QGP.

Relativistic Heavy-Ion Collider (RHIC) was built with the aim of creation and study of bulk matter made of deconfined quarks and gluons. The temperature and density in high energy heavy-ion collisions are expected to be similar to those which prevailed in the early universe, before the protons and neutrons were formed. The study of the properties of the matter created in these collisions enables physicists to answer important questions of nuclear physics, astrophysics and high-energy physics.

Particle production at large transverse momenta (p_T) in relativistic heavy ion collisions provides an important test for perturbative quantum chromodynamics, (pQCD).

This dissertation prospectus proposes to analyze experimental data taken by the STAR detector at RHIC during the year 2003 (experimental run 3) in order to measure neutral pion (π^0) yield in proton-proton (pp) and deutron-gold (dAu) collisions as a

function of transverse momentum.

Results from inclusive neutral pion production may provide meaningful constraints on the gluon-to-pion fragmentation [2]. p_T dependence of the ratio of π^0 yield in pp to that in dAu is important for understanding how π^0 yield scales with the number of nucleons participating in the collision.

Methods developed and employed in π^0 detection are useful in other areas of physics analysis. Background from π^0 must be subtracted in order to construct a p_T spectrum of direct photons. Large fraction of transverse energy (E_T) is carried by neutral pions. Partonic jets emerging from the collision region in the early stage fragment into hadron sprays in which the leading particle is often a π^0. Triggering on high p_T π^0 provides an efficient jet trigger.

The remainder of the prospectus is organized as follows. In Chapter 2, the underlying physics is discussed in more detail. In Chapter 3, the experimental setup is presented with the emphasis on STAR Barrel Electromagnetic Calorimeter (BEMC). Chapter 4 is the overview of the analysis methods and corrections, along with preliminary results.

Chapter 2

Physics

2.1 QCD

QCD is a well established theory confirmed by experimental data within its domain of applicability, namely strong interactions – the theory of interactions of quarks and gluons. According to QCD the effective coupling constant α_s is a decreasing function of the energy of the interaction. This leads to the intriguing concept of *asymptotic freedom* which postulates that at high energies quarks and gluons become effectively free. Hadronic collisions can be described to a high degree of accuracy by perturbative QCD (pQCD) (Figure 2.1).

While the High Energy experiments are capable of creating conditions at which quarks, gluons and various symmetries of QCD reveal themselves, High Energy nuclear experiments add the additional condition of high density. The behavior of nuclear matter at high temperature and density is especially interesting because the combination of high energy density and high temperature leads to the formation of a new state of matter known as the Quark Gluon Plasma (QGP).

2.2 High p_T particle ratios

High p_T hadrons created in relativistic heavy ion collisions arise from fragmentation of quarks and gluons (partons) scattered with large momentum transfer, Q^2, in the initial parton-parton interactions [4]. In the absence of nuclear medium effects, a

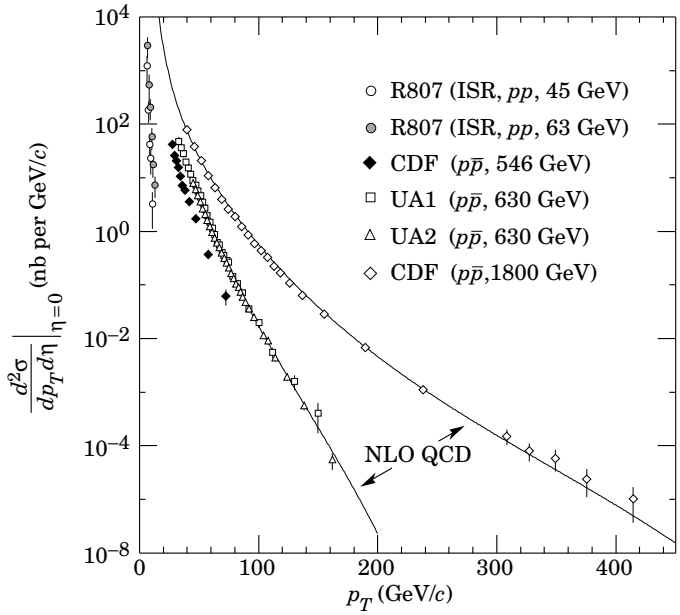

Figure 2.1: Differential cross sections for the observation of a single jet of pseudo-rapidity $\eta = 0$ as a function of the transverse momentum of the jet. The lines through the data are next-to-leading order (NLO) QCD curves for 630 GeV and 1800 GeV $p + \bar{p}$ collisions. Figure taken from the Particle Data Book [3].

collision of two nuclei would look like a superposition of nucleon-nucleon collisions [5]. High p_T particle yields in nuclear collisions would be same as in pp collisions (neglecting the isospin effects responsible for the difference between protons and neutrons), scaled by the average number of inelastic nucleon-nucleon collisions (binary scaling). One of the most interesting results from the experiments at the BNL Relativistic Heavy Ion Collider is the significant suppression of high p_T particle yields in $AuAu$ collisions compared to pp collisions at the same center-of-mass energy, scaled with the number of binary collisions [6], [7], [8], [9].

As partons propagate through the hot and dense matter created in nuclear collisions, they lose energy via gluon radiation (gluon bremsstrahlung) [10]. This process is also known as *jet quenching*. Theoretical calculations (pQCD) predict this energy loss (dE/dl) to be of the order of $1 - 3$ GeV/fm [11]. Thus, high p_T partons lose a significant portion of their momenta in the medium, resulting in suppression of high p_T hadron yields. Jet quenching is of great interest because it is sensitive to the final-state interactions that may lead to thermal and chemical equilibrium in the produced dense partonic system [10], [12].

Hard processes responsible for high p_T parton production are also sensitive to initial state nuclear effects. It is known from deep-inelastic scattering experiments that the quark structure functions with small ($x < 0.1$) fractional momenta are suppressed in a nucleus compared to a free nucleon [13]. This depletion, usually referred to as *nuclear shadowing*, leads to suppression of high p_T single-particle inclusive spectra. Nuclear shadowing is of interest because it significantly influences the initial conditions in high-energy nucleus-nucleus collisions. Another initial state process that affects high p_T particle yield is soft scattering of the incident parton prior to its hard scattering (Cronin effect).

A vital question for interpretation of experimental data is whether suppression of high p_T hadrons spectra is due to the initial or final state effects. In order to disen-

tangle and quantitatively describe these effects, it is necessary to create experimental conditions at which only one class of the effects is present while the other one is not. Such conditions can indeed be satisfied in proton-nucleus (pA) and deutron-nucleus (dA) collisions. Initial state effects, including nuclear modifications to the parton structure functions and soft scatterings, should be present in pA, dA and AA collisions, whereas only high p_T partons resulting from AA collisions are subject to the final-state jet quenching. Hence, to gain access to the information about jet quenching from high-energy AA collisions, it is imperative to experimentally determine the modification (if any) of high p_T hadron yields due to initial-state nuclear effects for a system in which a hot, dense medium is not produced in the final state [5]. The absence of such modification would indicate that the observed suppression in high p_T particle yields in $AuAu$ collisions is due to jet quenching, providing important information about the system produced.

Medium effects on high p_T production in dAu collisions are quantified by the modification factor R_{dA} defined as a ratio of the measured dAu invariant yield to the scaled pp invariant yield:

$$R_{dAu}(p_T) = \frac{(1/N_{dA}^{evt})d^2N_{dA}/d\eta dp_T}{\langle N_{coll}\rangle/\sigma_{pp}^{inel} \times d^2\sigma_{pp}/d\eta dp_T}, \tag{2.1}$$

where the $\langle N_{coll}\rangle$ is the average number of inelastic nucleon-nucleon collisions per event in the minimum bias collisions, and $\langle N_{coll}\rangle/\sigma_{pp}^{inel}$ is the nuclear overlap function $\langle T_{dA}(b)\rangle$. Using a Glauber model $\langle N_{coll}\rangle$ is 8.5 ± 0.4 in minimum bias dAu collisions [5].

The inclusive charged hadron yield in dAu measured by STAR collaboration [14] indicates that there is no suppression of high p_T particles relative to binary-scaled pp collisions (Figure 2.2). The enhancement at $p_T > 2$ GeV was observed in earlier $p + A$ experiments [15] and is generally referred to as the "Cronin effect".

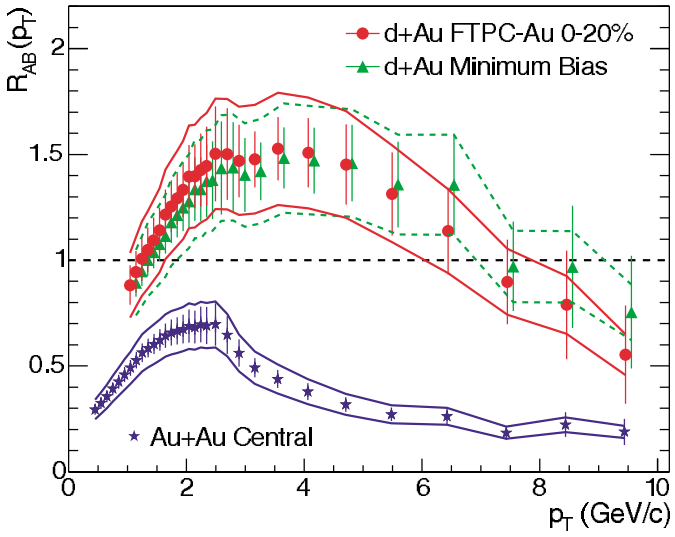

Figure 2.2: $R_{AB}(p_T)$ for minimum bias and central dAu collisions, and central $AuAu$ collisions. The minimum bias dAu data are displaced 100 MeV/c to the right for clarity. The bands show the normalization uncertainties.

2.3 Neutral Pions

The invariant cross section for a given process is an important observable to help establish the dynamical origin of particle production [16]. One of the most well-defined and understood hadronic interactions is the production of neutral pions from pp collisions. In this reaction the simplest possible (stable) hadronic target and projectile react and form the simplest possible hadronic product (π^0). For experimental reasons the outgoing pion can be measured over a wider energy range than any other particle, thus providing a commensurably larger kinematic range for comparison with theory. The history of pion cross section measurements and their comparison with theory is illustrated in Figure 2.3. These data, spanning some 11 orders of magnitude, summarize the results from major proton experiments over the past 25 years. The center-of-mass energy of these experiments increases an order of magnitude from about 20 GeV to 200 GeV. While next-to-leading order perturbative QCD (NLO pQCD) calculations underpredict measured cross section for π^0 production by nearly

an order of magnitude for the lowest center-of-mass energy $\sqrt{s}$ = 19.4 GeV, the agreement becomes increasingly better at higher $\sqrt{s}$.

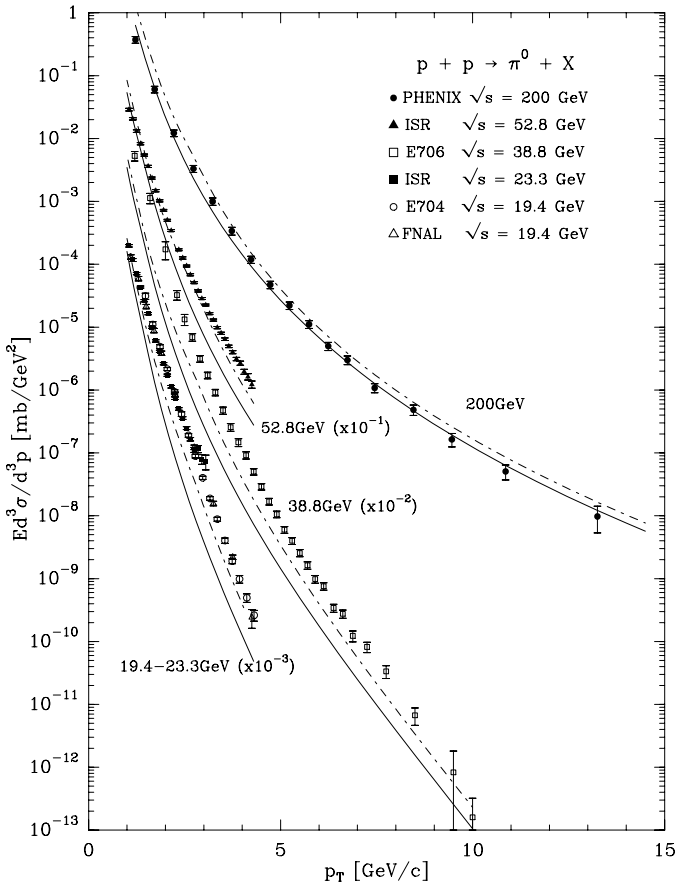

Figure 2.3: $Ed^3\sigma/d^3p$ at 90° and various energies, as a function of p_T. The curves are the corresponding NLO pQCD calculations with $\mu = p_T$ (solid lines) and $\mu = p_T/2$ (dotted-dashed lines), where μ is a factorization scale associated to the running strong coupling constant α_s. Figure taken from [17].

The ratio Data/Theory suggests that at lower $\sqrt{s}$ neutral pion production mechanism is dominated by soft processes. The relative size of the soft contributions increases in the forward direction, where the disagreement between data and pQCD gets larger [17]. However, neutral pion cross section at large rapidity in pp collisions at $\sqrt{s} = 200$ GeV measured by STAR (Figure 2.4) is in a good agreement with the NLO pQCD calculation. This agreement suggests that particle production at large

forward rapidity at $\sqrt{s} = 200$ GeV is predominantly due to partonic scattering, rather than soft mechanisms presumed responsible for beam fragmentation.

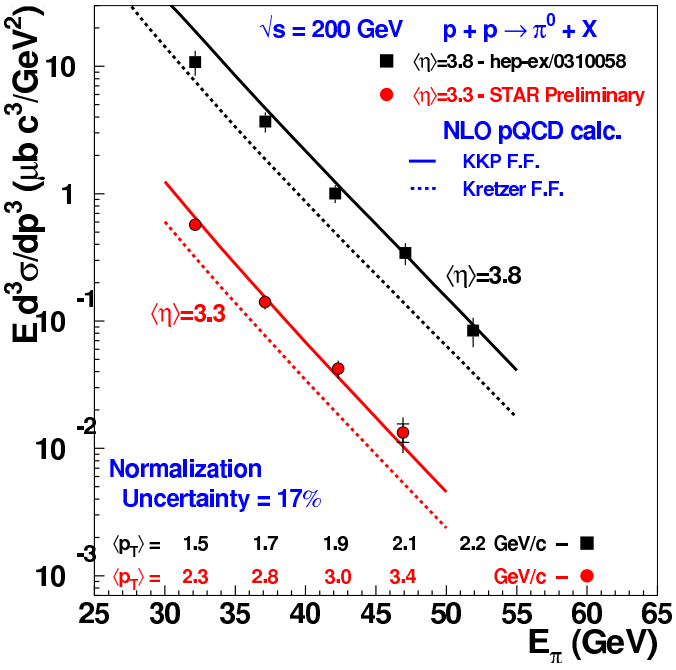

Figure 2.4: Invariant cross section for neutral pions produced in pp collisions at $\sqrt{s} = 200$ GeV. The cross section points are shown versus the average energy of the pion, detected at fixed pseudorapidity by the Forward Pion Detector (FPD) at STAR. Figure taken from [16].

The ratio R_{dAu} for π^0 measured by PHENIX collaboration (Figure 2.5) shows that there is no suppression of high p_T neutral pions in dAu relative to binary-scaled pp collisions [5]. Thus, nuclear medium effects are not present in dAu collisions and high p_T suppression observed in $AuAu$ is due to jet quenching (and not the initial state effects).

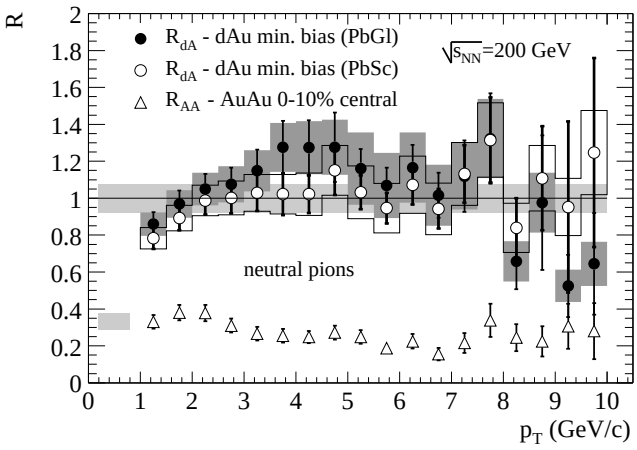

Figure 2.5: R_{dAu} for π^0 in the PbGl and PbSc calorimeters in minimum bias dAu. The bands around data show systematic errors which can vary with p_T, while the shaded band around unity indicates the normalization uncertainty. The nuclear modification factor R_{AA} in 10% most central collisions is also shown.

Chapter 3

The Experiment

3.1 RHIC

Relativistic Heavy Ion Collider is located at Brookhaven National Laboratory (BNL). It is designed to accelerate and provide collisions between two beams of heavy ions, deutrons and protons, and any combination of them. This diversity allows the study of colliding systems as a function of both energy an system size. RHIC characteristics are summarized in Table 3.1.

RHIC is a large step forward in terms of energy per nucleon, compared to previously built colliders capable of accelerating beams of heavy ions. The summary of existing and future heavy ion colliders and their key characteristics is given in Table 3.2.

Accelerator complex at BNL, required to produce, accelerate and store the heavy ion beam, consists of the Tandem Van de Graaff accelerators, the Booster Synchrotron and the Alternating Gradient Synchrotron (AGS) (Figure 3.1). Gold (Au) atoms with a charge $Q = -1$ are generated in the Pulsed Sputter Ion Source in the Tandem Van de Graaff facility, accelerated and passed through two layers of Au foil, leaving the Au atoms with a net charge $Q = +32$. The Au beam of 1 MeV/nucleon energy is transferred to the booster where it is accelerated to 95 MeV/nucleon and then stripped to a net charge $Q = +77$. In the AGS, the Au beam is bunched and further accelerated to 10.8 GeV/nucleon and is extracted using fast extraction. Fast

Physical Parameters		
RHIC circumference (m)	3833.845	
No. Intersection Regions	6	
No. Bunches/ring	60	
Bunch Spacing (nsec)	213	
Collision Angle	0	
Free Space at Crossing Point (m)	± 9	
Performance Specifications	Au	p
No. Particles/Bunch	1×10^9	1×10^{11}
Top Energy (GeV/u)	100	250
Luminosity, average ($cm^{-2}sec^{-1}$)	$\sim 2 \times 10^{26}$	$\sim 1 \times 10^{31}$

Table 3.1: Physical parameters and performance specifications for the Relativistic Heavy Ion Collider (RHIC).

	AGS	AGS	SPS	SPS	SPS	RHIC	RHIC	LHC
Start year	1986	1992	1986	1994	1999	2000	2001	2006
A_{max}	^{28}Si	^{197}Au	^{32}S	^{208}Pb	^{208}Pb	^{197}Au	^{197}Au	^{208}Pb
E_P^{max} [AGeV]	14.6	11	200	158	40	0.91E4	2.1E4	1.9E7
$\sqrt{s_{NN}}$ [GeV]	5.4	4.7	19.2	17.2	8.75	130	200	6000
$\sqrt{s_{AA}}$ [GeV]	151	934	614	3.6E3	1.8E3	2.6E4	4E4	1.2E6
$\Delta y/2$	1.72	1.58	2.96	2.91	2.22	4.94	5.37	8.77

Table 3.2: RHIC compared to existing and future facilities; A_{max} is the maximum species mass number, E_P^{max} is the maximum (equivalent) fixed-target beam energy per nucleon, $\sqrt{s_{NN}}$ is the maximum center of mass energy, and $\Delta y/2$ is the rapidity gap from the beam to mid-rapidity [18].

Extracted Beam (FEB) extracts many AGS Au bunches into one RHIC bunch. The FEB bunches are then injected into RHIC rings through the AGS to RHIC (ATR) transfer line. At this stage the Au nuclei are completely stripped of electrons and have a charge of $Q = +79$. In RHIC, the bunches are accelerated to collision energy and stored for data taking.

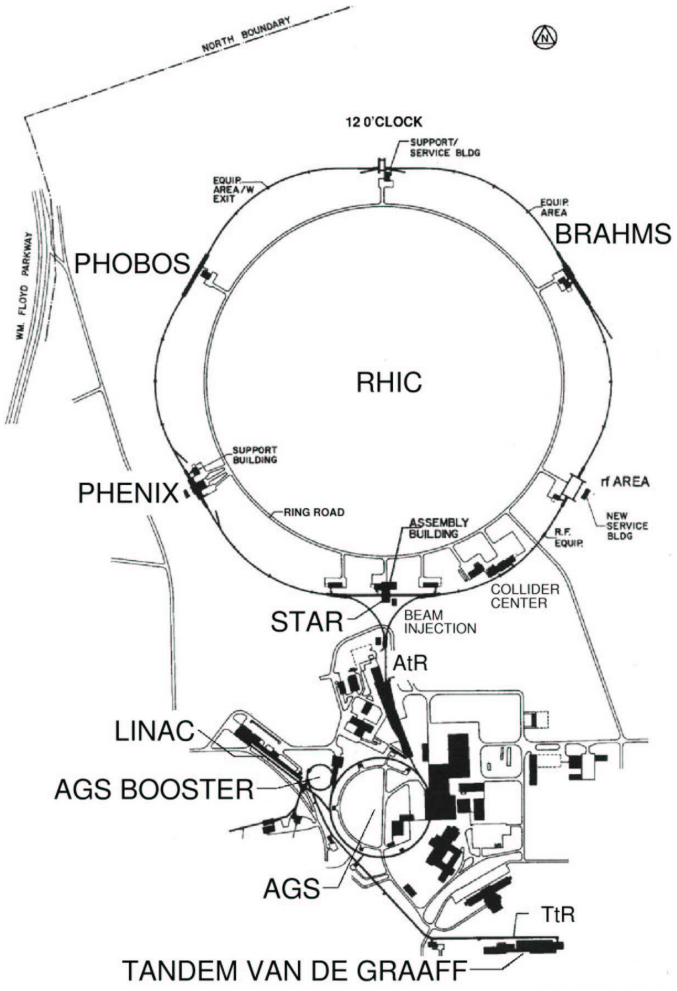

Figure 3.1: Brookhaven National Laboratory collider complex including the accelerators that bring the nuclear ions up to RHIC injection energy (10.8 GeV/u for $^{197}Au^{79}$

RHIC consists of two rings of superconducting magnets (Figure 3.2), each with a circumference of 2.4 miles. The magnets are cooled by circulating liquid helium to

a temperature of less than 4.6 K. Extremely good vacuum inside the beam pipes is necessary to minimize beam losses and radiation background. Vacuums achieved in the cold and warm sections of RHIC are $\sim 10^{-11}$ mbar and $\sim 10^{-10}$ mbar respectively.

RHIC provides particle collisions at 6 intersection regions located around the collider ring, with 4 of them presently occupied by two large (STAR, PHENIX) and two smaller (BRAHMS, PHOBOS) experiments.

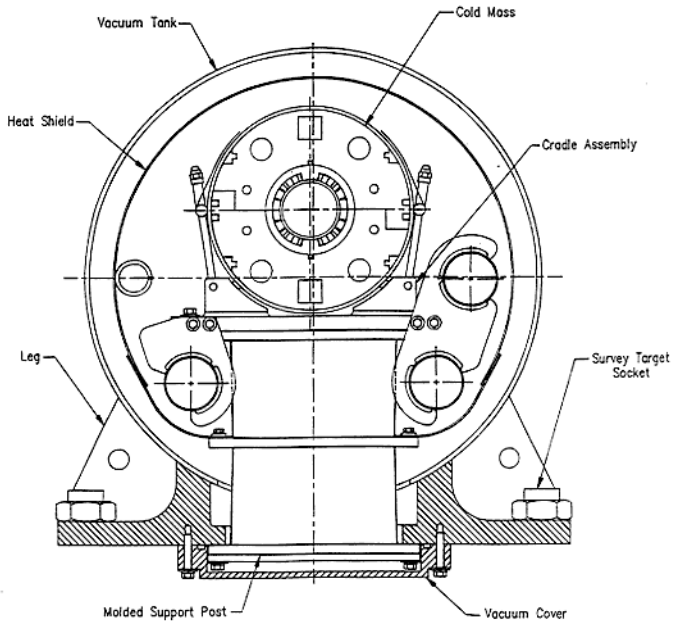

Figure 3.2: Cross section of an arc dipole. The outer diameter of the vacuum vessel is 610 millimeters.

3.2 STAR

STAR stands for "Solenoidal Tracker at RHIC" (Figure 3.3) and gets its name from the large tracking detector (Time Projection Chamber, or TPC) located in the center of the detector. STAR is an azimuthally symmetric, large acceptance, solenoidal detector designed to measure many observables simultaneously in high multiplicity heavy ion collisions. The detector consists of many subsystems, many of which are located inside a 0.5 Tesla solenoidal magnet (Figure 3.4).

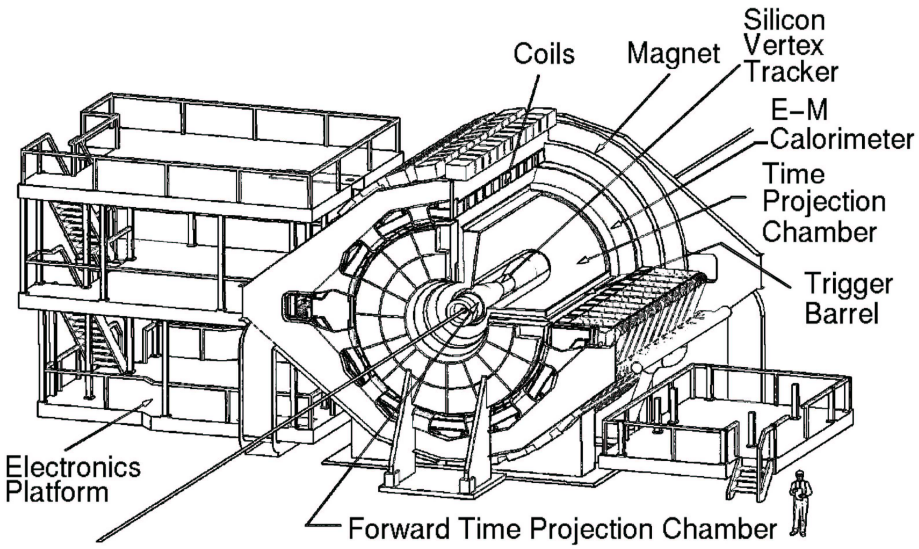

Figure 3.3: View of the STAR detector. Figure taken from [19].

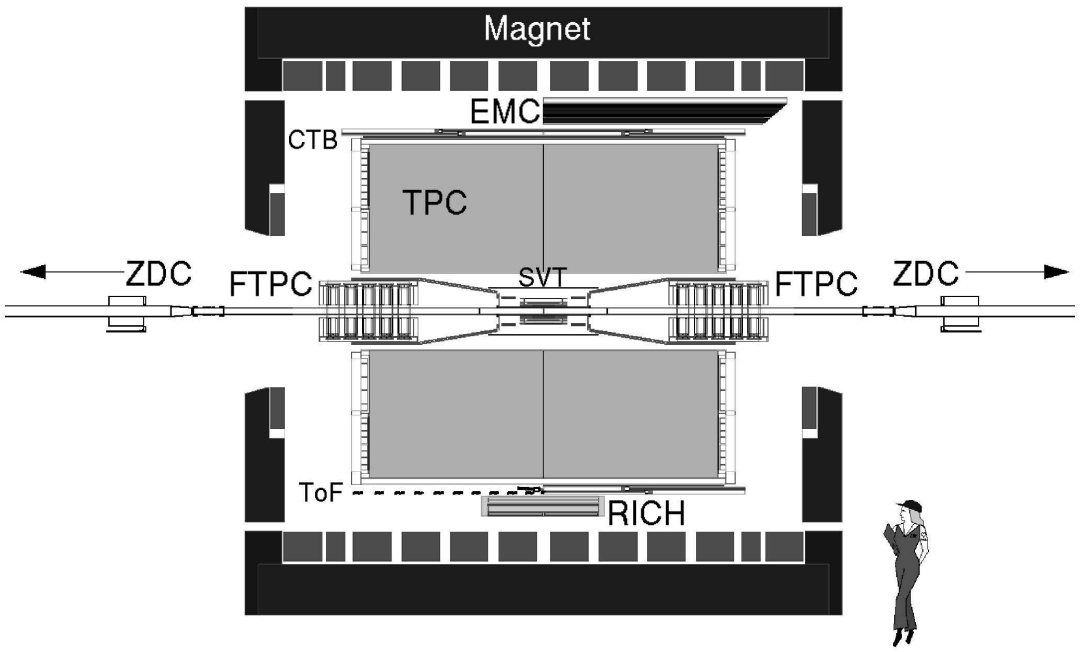

Figure 3.4: Cutaway of the STAR detector in its 2001 configuration; including a partial installation of the electromagnetic calorimeter (EMC), the temporary ring-imaging Cherenkov detector (RICH), and a time-of-flight detector (ToF) prototype.Figure taken from [19].

The TPC is STAR's main detector that can track $\sim 4 \times 10^3$ charged particles. The TPC covers the pseudorapidity region $|\eta| < 1.8$. It can measure particle p_T within the approximate range $0.07 < p_T < 30$ GeV. The momentum resolution depends on η and p_T of the track but for most tracks $\delta p/p \sim 0.02$.

3.3 STAR Barrel EMC

3.3.1 Mechanical Structure

STAR Barrel EMC is a sampling calorimeter and consists of layers of lead and scintillator (a complete description can be found in [20]). It covers more than 100 m^2 of area outside the TPC for $|\eta| < 1$. Barrel calorimeter includes a total of 120 calorimeter modules, each subtending 6^0 in ϕ (0.1 radian) and 1.0 unit in η. The modules are mounted 60 in ϕ by 2 in η (Figure 3.5). Each module is $\sim$ 26 cm wide by $\sim$ 293 cm long with an active depth of 23.5 cm ($21X_0$) and about 6.6 cm in structural plates (of which 1.9 cm lies in front of the detector). A module is further divided into 40 towers, 2 in ϕ and 20 in η, with each tower being 0.05 in $\Delta\phi$ by 0.05 in $\Delta\eta$. The calorimeter thus is physically segmented into a total of 4800 towers, each of which is projective and pointing back to the interaction diamond. Figure 3.6 shows a side view of a module illustrating the projective nature of the towers in η-direction.

Each module consists of a lead-scintillator stack and shower maximum detectors located $\sim$ 5 radiation lengths from the front of the stack (Figure 3.6). There are 20 layers of lead and 21 layers of scintillator. Lead layers are 5 mm thick; 2 layers of scintillator located in front of the stack and used in the preshower detector are 6 mm thick, and the remaining 19 scintillator layers are 5 mm thick. The stack is held together by 30 straps connecting the non-magnetic front and back plates of a calorimeter module. Figure 3.7 shows an end view of a module along with the mounting system and the compression components.

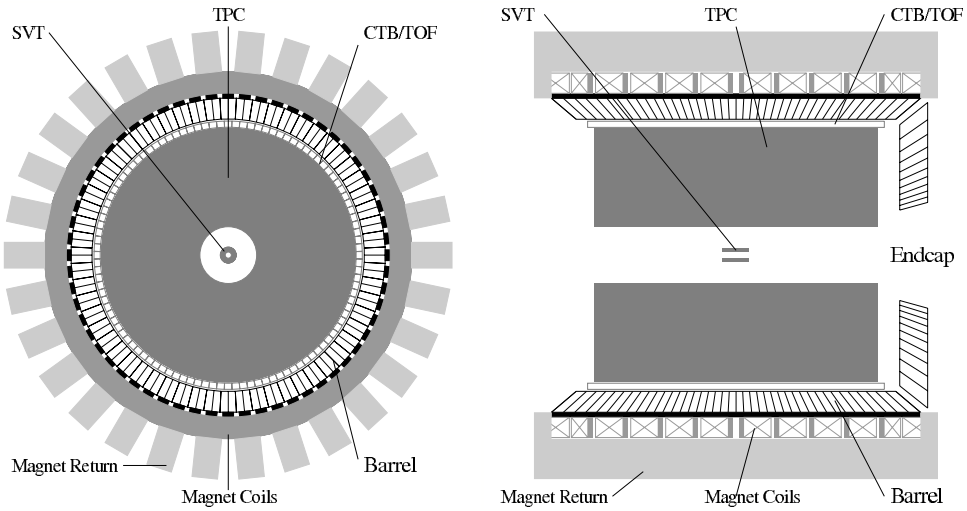

Figure 3.5: Cross sectional view of the STAR detector. The barrel EMC covers $|\eta| < 2$ and 2π in azimuth.

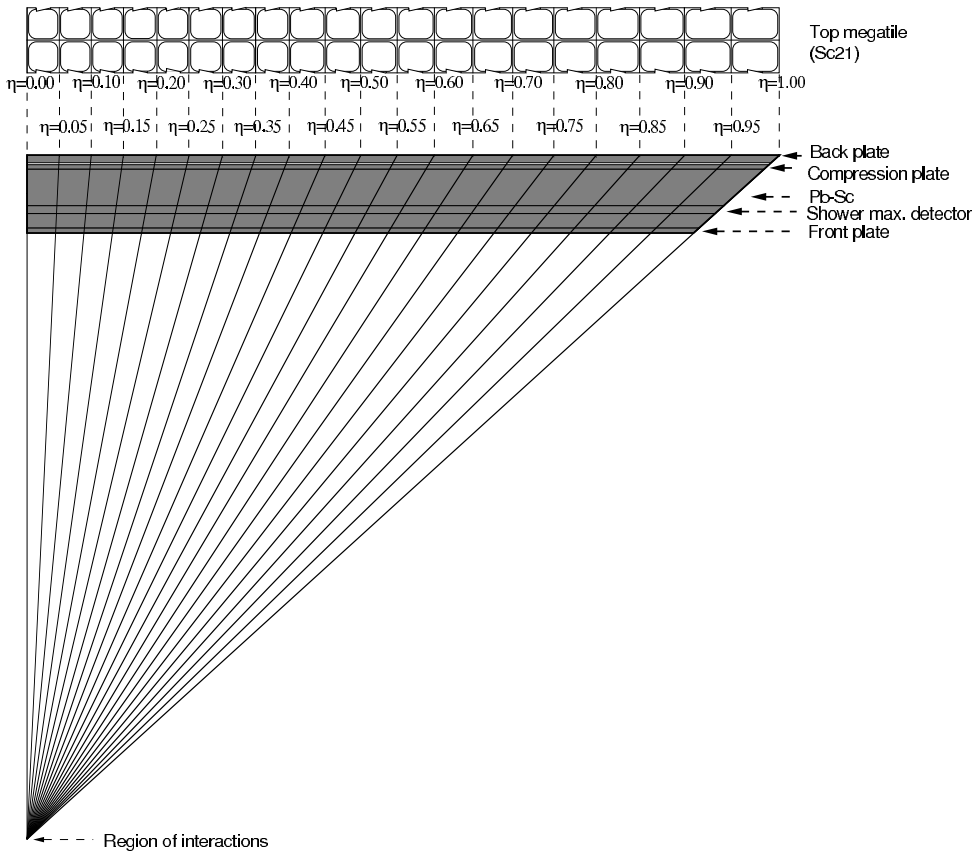

Figure 3.6: Side view of a calorimeter module showing the projective nature of the towers. The 21^{st} megatile layer is also shown.

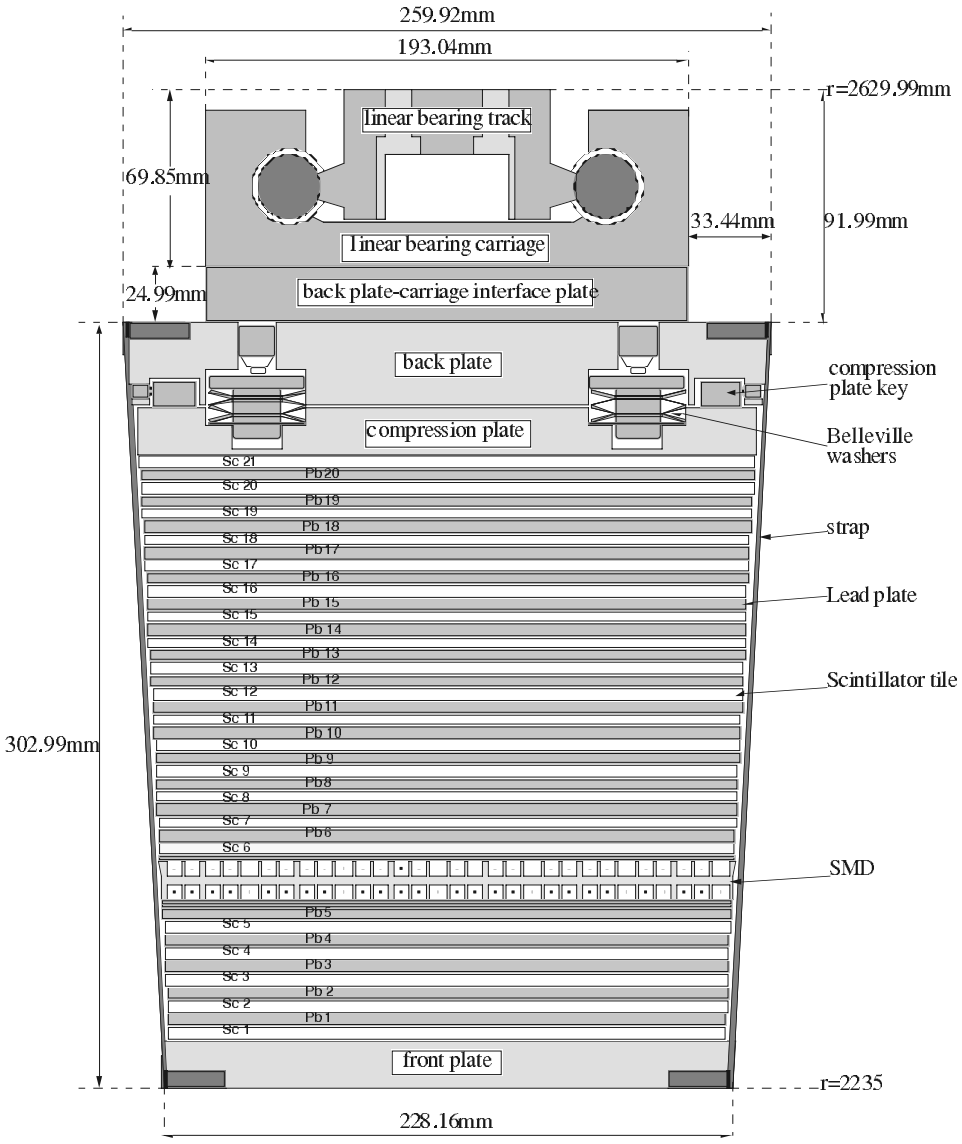

Figure 3.7: End view of a calorimeter module showing the mechanical assembly including the compression components and the rail mounting system. Shown is the location of the two layers of shower maximum detector at a depth of approximately $5X_0$ from the front face at $\eta = 0$.

3.3.2 The STAR BEMC Optical Structure

There are 21 active scintillating layers in the barrel calorimeter. The scintillator layers alternate with 20 layers of lead absorber plates. The plastic scintillator layers are manufactured in the form of "mega-tile" sheets with 40 optically isolated area segments ("tiles") in each layer. The layout of the 21^{st} mega-tile sheet is illustrated in figure 3.6. The signal from each scintillating tile is read-out with a wavelength shifting (WLS) fiber embedded in a "σ-groove" that is machined in the tile (Figure 3.8). The optical isolation between individual tiles in a given layer is achieved by carving 95% of the depth through the scintillator sheet and filling the resulting groove with opaque, silicon dioxide loaded epoxy. The potential optical cross talk between adjacent tiles as a result of the remaining 5% of the scintillator thickness is cancelled to the level of $< 0.5\%$ by a thin black line painted at the location of the isolation grooves on the uncut scintillator surface.

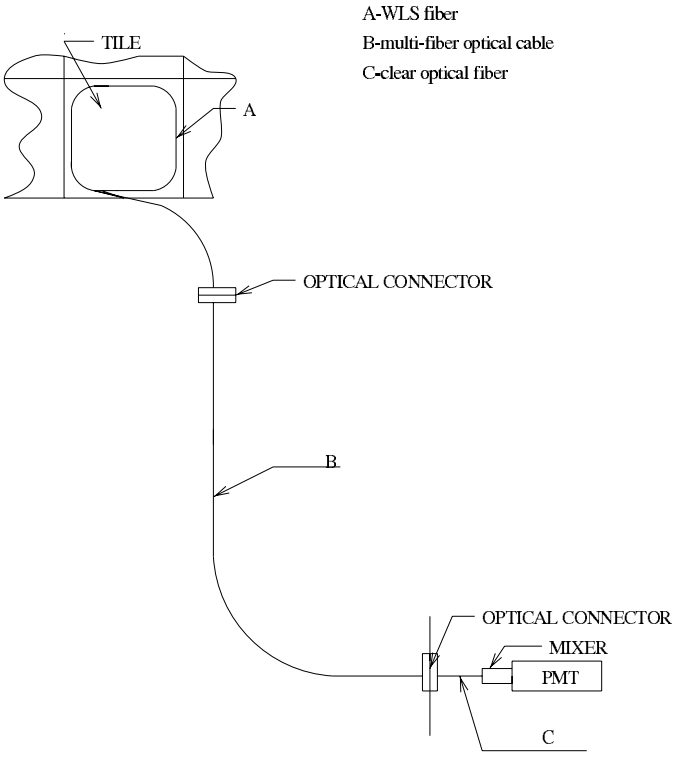

Figure 3.8: A diagram of tile/fiber optical read-out scheme of Barrel EMC.

A total of 840 different tile shapes (420 plus their mirror image) were machined in the layers of each module. The machined, unpolished mega-tile edges are painted white with Bicon BC620 reflective paint. White bond paper, which has good diffuse reflectivity and, most important, a high coefficient of friction, is used on both surfaces of the mega-tile as a diffuse reflector between calorimeter layers.

After exiting the scintillator the WLS fiber is routed along the outer surface of the lead scintillator stack, under the module's light tight cover and terminate in a multi-fiber optical connector at a back-plate of module. A 2.1 m long multi-fiber optical cable of clear fibers connected with mating optical connectors, carries the light from the optical connector through the magnet structure to decoder boxes mounted on the outer surface of the STAR magnet, where the light from 21 tiles composing a single tower is merged onto a single photo multiplier tube (PMT).

The photo multiplier tubes used for the EMC towers are Electron Tube Inc. model 9125B. PMT's are powered by Cockroft Walton bases that are remotely controlled by the slow control software written in LabView.

3.3.3 Shower Maximum Detector

A shower maximum detector (SMD) is used to provide fine spatial resolution in a calorimeter which has segmentation (towers) significantly larger than an electromagnetic shower size. While the barrel EMC towers provide presice energy measurements for isolated electromagnetic showers, the high spatial resolution provided by the SMD is essential for π^0 reconstruction, direct γ identification, and electron identification. Information on shower position, shape, and, from the signal amplitude, the electromagnetic shower longitudinal development are provided.

Figure 3.9 shows the conceptual design of the STAR BEMC SMD. It is located $\sim$ 5 radiation lengths deep in the calorimeter modules at $\eta = 0$ including all ma-

terial immediately in front of the calorimeter[1]. A two sided aluminum extrusion provides ground channels for two independent planes of proportional wires. Independent printed circuit (PC) board cathode planes with strips etched in the η and ϕ directions respectively allow reconstruction of a two dimensional image of the shower as shown schematically in Figure 3.9.

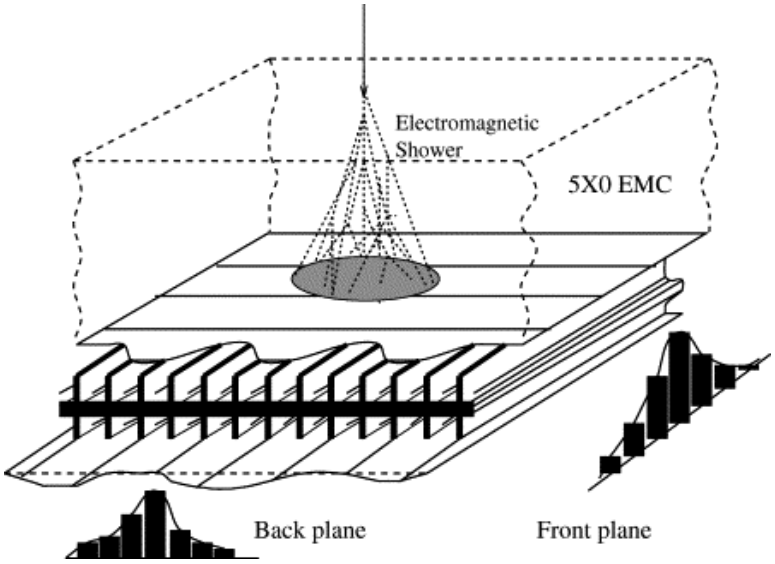

Figure 3.9: Schematic illustration of the double layer STAR BEMC SMD. Two independent wire layers separated by an aluminum extrusion image electromagnetic showers in the η and ϕ directions on corresponding pad layers.

The SMD is a wire proportional counter – strip read out detector using gas amplification. The basic structure of the detector is an aluminum extrusion with 5.9 mm wide channels running in the η direction. A cross sectional view of the detector is shown in Figure 3.10 and the design parameters are summarized in table 3.3.

In the center of the extrusion channels there are 50 μm gold plated tungsten wires. The detector strips sense the induced charge from the charge amplification near the wire. Strips perpendicular to the wires provide an image of the shower spatial

[1]The depth of the shower maximum detector varies from $4.6X_0$ to $7.1X_0$ counting only the calorimeter material as η varies from 0 to 1

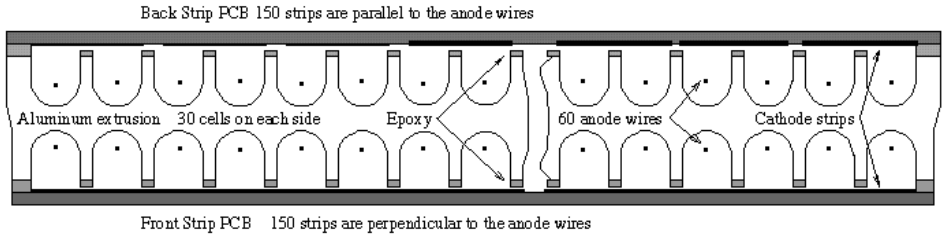

Figure 3.10: Cross sectional view of the SMD showing the extruded aluminum profile, the wires and cathode strips.

distribution in the η direction. The other set of strips is parallel to the wires; these provide shower coordinate measurements in ϕ direction. Signals from the cathodes propagate along a transmission line plane in the printed circuit boards to reach the front end electronics (FEE) board. At the FEE board, amplified cathode strip signals are buffered in a switched capacitor array before being multiplexed 80 : 1 to external digitizer crates mounted outside the STAR magnet.

3.3.4 Preshower Detector

The first two scintillating layers of the calorimeter have separate readout fibers. The scintillation light from these two layers of each tower is brought to the multi anode phototubes located in the PMT decoder boxes. A total of 300, 16 pixel multi anode PMT's are used to read 4800 fiber pairs providing the tower preshower signals. Preshower readout electronics was not installed until the RHIC physics run IV.

3.3.5 BEMC Electronics

The BEMC electronics includes trigger, readout of phototubes and SMD, high voltage system for phototubes, low voltage power, slow controls functions, calibration controls, and interfaces to the STAR trigger, DAQ dnd slow controls. Front end electronics including signal processing, digitization, buffering, formation of trigger primitives, and the first level of readout is located in custom EMC crates located on

SMD Design Parameters	
Chamber Position Inside EMC	$\sim 5X_0$ at $\eta = 0$
Rapidity Coverage (Single Module)	$\Delta\eta = 1.0$
Azimuthal Coverage (Single Module)	$\Delta\phi = 0.105$ (6^0)
Occupancy (pp)	$\approx 1\%$
Occupancy ($AuAu$)	> 5 to $\sim 25\%$
Chamber Depth (Cathode to Cathode)	20.6 mm
Anode Wire Diameter	50 μm
Gas Mixture	90%-Ar / 10%-CO_2
Gas Amplification	~ 3000
Signal Length	110 ns
Strip Width (Pitch) in η for $\|\eta\| < 0.5$	1.46 (1.54) cm
Strip Width (Pitch) in η for $\|\eta\| > 0.5$	1.88 (1.96) cm
Strip Width (Pitch) in ϕ	1.33 (1.49) cm
Number of Strips per Module	300
Total Number of Modules	120
Total Number of Readout Channels	36000

Table 3.3: STAR Barrel EMC SMD Design Parameters.

the outside of the magnet iron. SMD front end electronics including preamplifiers and switched capacitor arrays reside on the EMC modules inside the STAR magnet.

In STAR trigger hierarchy, level-0 (L0) consists of that detector information available, without dead time, at each RHIC crossing. L0 is different from all higher levels in that it selects events for processing while all other trigger levels only function as event aborts. BEMC is an important part of STAR L0 trigger, capable of triggering on high p_T physics through its electromagnetic component. STAR jet trigger relies largely on leading π^0's in the BEMC with some contribution from the significantly smaller energy deposition of hadronic showers.

In STAR, L0 is the only trigger level which does not incur large dead times associated with the opening of the gated grid in the TPC. For all practical purposes L0 is deadtimeless and capable of selecting events on each RHIC beam crossing. The TPC grid cycling rate is limited which makes it very important to concentrate as much functionality as possible in L0 trigger. The STAR L0 trigger must provide a trigger to the TPC within 1 μsec ($\sim$ 10 RHIC beam crossings) and to the STAR L0 trigger processors within about 700 ns, including cable delays. For reasons of speed and limited bandwidth, the EMC trigger uses trigger primitives instead of the full EMC data. There are two kinds of trigger primitives formed by the EMC front end electronics. The first set of primitives called "high tower trigger" is 300 high tower values of 6 bits from the single largest tower ADC within each 4×4 patch of 16 towers. The second set of primitives called "patch trigger" is 300 tower sums, digitized to 6 bits each, from patches of 4×4 towers. These primitives are processed to make a trigger decision on total E_T, jet triggers, γ triggers, etc. These results are then passed to STAR L0 in 700 ns to participate as a component of the final L0 decision.

The BEMC tower data is processed via a separate patch. The PMT signals from the towers are integrated and digitized in the front-end cards on every RHIC crossing. These data are pipelined until L0 trigger time, and if a trigger occurs are transferred

to a token-addressable memory on the card to await readout.

The signals from the pads of the SMD are amplified by the FEE cards before entering an analog pipeline composed of switched capacitor arrays to await the L0 trigger. Upon L0 trigger, the SMD analog signals are queued with multiplexing ration of $80:1$ to the 10 bit SMD digitizer crates located outside the STAR magnet. SMD digitized signals are first available in STAR L2 trigger processors in ~ 200 μsec, well ahead of digital information from the TPC.

Chapter 4

Analysis

4.1 Neutral Pion Reconstruction

While charged particles are detected using tracking detectors, π^0 is detected using electromagnetic calorimetry via $\pi^0 \rightarrow 2\gamma$ decay channel. Neutral pion decays into a pair of photons 98.8% of the time, making it the most convenient decay channel for π^0 reconstruction. Positions and energies of the daughter photons are determined using the Barrel EMC, and the interaction vertex ("primary vertex") is determined by finding the common origin of the TPC tracks. This information completely describes kinematics of the decay. Invariant mass of the π^0 is found as:

$$m_{\gamma\gamma} = \sqrt{2E_1E_2(1 - cos\theta)}, \tag{4.1}$$

where E_1, E_2 are the energies of the daughter photons, and θ is the opening angle.

When a particle hits BEMC, it has certain probability to deposit some fraction (possibly all) of its energy in different parts of the calorimeter: preshower[1], SMD, and sampling towers. Clustering is done independently for towers and SMD η- and ϕ-planes. Clusters are then matched together to form BEMC *points*, from which energies and coordinates of photon candidates are determined. A histogram is filled with invariant mass values of pairs of BEMC points calculated using 4.1. With certain cuts applied, the π^0 mass peak can be seen close to its known value, $m_{\pi^0} =$

[1]Preshower information was not available for *pp* and *dAu* runs and is not used in this analisys

134.9766 ± 0.0006 MeV (Figure 4.1). The signal/background ratio may be quite low due to high combinatoric background, statistical uncertainties, and uncertainties in determining the energies and coordinates. Neutral pion mass peak reconstruction becomes especially challenging at at higher p_T, where statistics is limited and the experimental uncertainties are large due to the cluster merging.

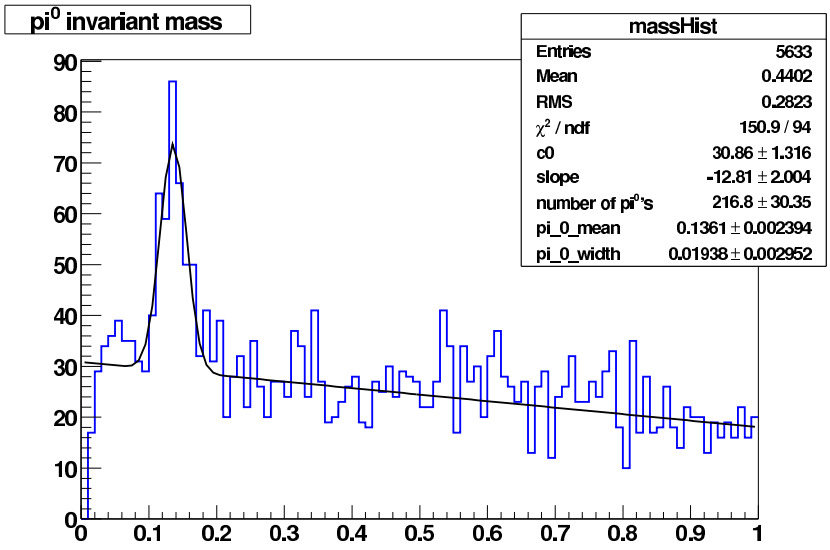

Figure 4.1: Invariant mass distribution (1 GeV units) of pairs of points in pp events, fitted with a straight line and a Gaussian. π^0 mass peak is clearly seen.

4.2 Neutral Pion Yield

In order to extract π^0 yield vs. p_T, the invariant mass distributions are constructed for different p_T bins. To separate signal from background, two different methods can be employed, i.e. mixed events and fitting method. Fitting the background is a more straightforward method but has a disadvantage of ambiguity in choosing the fitting function and the subrange to fit. Mixed events method is based on the idea that BEMC points in two different events are uncorrelated, thus the background may be reproduced by building invariant mass distributions using points taken from different events of similar multiplicity. While reproducing the background accurately

at $m > 0.3$ GeV, this method fails to reproduce the lower part of invariant mass spectrum ($m < 0.1$ GeV), where the background shape is determined by "cluster splitting". Cluster splitting occurs when a single tower cluster energy is split between two SMD clusters according to their energies. Split clusters have high uncertainty in energy due to the poor energy resolution in the SMD. Signal from the split clusters is highly correlated with the signal from π^0, especially at higher p_T where the opening angle between daughter photons becomes small. Mixed events method produces the invariant mass spectrum of uncorrelated pairs of points and for this reason does not reproduce the lower part of the spectrum well. The choice was made to use the spectrum fit as a method of extracting the signal.

In order to increase the statistics for high p_T part of π^0 spectrum, high tower trigger was employed during the data taking. Minimum bias event rate was *prescaled* (suppressed) in order to accept more rare HighTower-1 triggers. HighTower-1 triggered event rate was in turn prescaled to accept HighTower-2 triggers. The thresholds for the triggers were set at 8 (turning on at 9) and 13 (turning on at 14) ADC counts respectively. One trigger ADC count was equivalent to ~ 0.4 GeV in transverse energy. Raw π^0 yield is shown in Figure 4.2.

4.3 Corrections To Raw Yield

Raw π^0 spectrum must be corrected to account for different factors that affect probability of reconstructing a π^0. These factors can be subdivided into two categories: those having to do with detector acceptance, and those due to the reconstruction efficiency. Acceptance of the BEMC is not a continuous patch in pseudorapidity η and azimuthal angle ϕ, but rather a complicated structure with cracks between the modules, dead areas, noisy channels, etc. Efficiency of π^0 reconstruction is affected by both hardware and software. Hardware factors are related to the probability of a daughter photon to deposit energy in BEMC tower and SMD layers, energy and co-

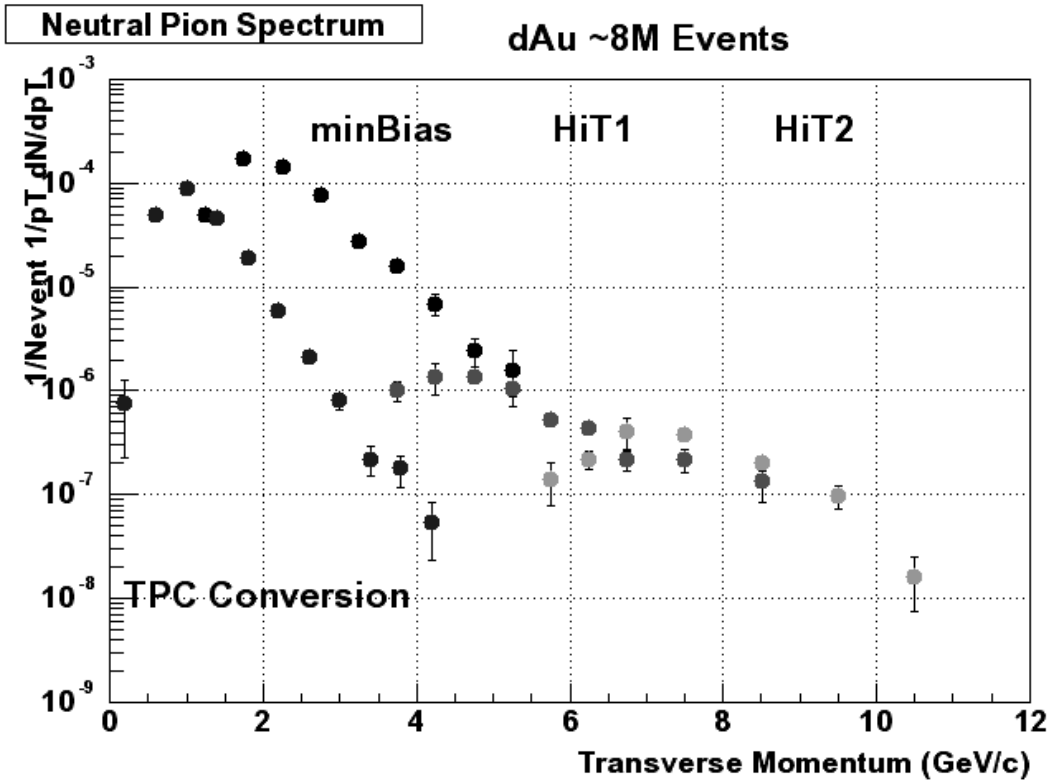

Figure 4.2: Uncorrected neutral pion yield vs. p_T in dAu (preliminary). Data points at low p_T are affected by software thresholds of the cluster finder. Data points at p_T close to the high tower trigger thresholds are affected by trigger efficiencies.

ordinate resolution, as well as being selected by the trigger. Software factors include cluster finder and point maker efficiencies, primary vertex reconstruction efficiency, and fits to signal and background.

Efficiency and acceptance effects are so tightly interrelated that it is practically inconceivable to distinguish the two. It is possible however to estimate the gross factor of efficiency and acceptance effects using Monte Carlo simulations. The method of Monte Carlo simulations is a powerful tool capable of giving the answer to the question of interest, namely, given a π^0 and assuming its momentum and coordinates are known, what is the probability that it will be detected and recognized as a π^0 in the invariant two-photon mass spectrum constructed from many events?

In order to account for background effects, a π^0 is embedded into a real event. Embedding is done by first simulating the kinematics of a π^0 decay using the primary vertex position taken from the real event. The detector response is then simulated using realistic detector geometry and electronics characteristics (digitization algorithm, noise, etc.). Simulated signals from all the detectors are then superimposed on the detector signals obtained from the real event. The event constructed this way is put through the reconstruction chain identical to the chain used for the reconstruction of real events. All information about the embedded π^0 and its decay products is stored separately and is available for further analysis. The essential assumption of this method is that the background event remains undisturbed by the introduced (embedded) signal, meaning the shapes of various distributions characteristic of the event are preserved.

At this stage of analysis, 46 thousand dAu minimum bias events were embedded with 1 π^0 per event with the following kinematic constraints:

- Uniform pseurorapidity window, $-0.3 < \eta < 1.3$ covering the detector acceptance for primary vertex positions $|\eta| < 60$ cm
- Full azimuthal coverage $-\pi < \phi < \pi$

- Flat p_T distribution from 1 to 12 GeV

Each of the π^0 daughter photons was matched to the BEMC point (if any) within a cone of radius 0.05 in η and ϕ around the "γ track" (information about γ track is known from the simulations). Angle of 0.05 is equal to the angular size of one BEMC tower. If there was more than 1 point within the specified cone, the track was matched to the closest point in η and ϕ.

In order to account for "p_T smearing" effect, the flat p_T spectrum of embedded π^0 was scaled according to the steeply falling charged hadron $\frac{h^+ + h^-}{2}$ p_T spectrum measured by STAR [14]. The p_T smearing effect mentioned above can be illustrated with help of the following example. A π^0 of given p_T can be reconstructed with transverse momentum greater or lesser than its p_T. The real π^0 spectrum is steeply falling, thus leading to a substantial "leakage" of lower-p_T π^0's to higher-p_T bins, whereas the leakage to lower-p_T bins is negligible. Thus, each π^0 was associated with a weight calculated according to the $\frac{h^+ + h^-}{2}$ p_T spectrum (Figure 4.3).

Invariant mass was constructed using pairs of BEMC points if matching γ tracks were found for both points. Each entry into the invariant mass histogram was weighted according to the spectrum shown in Figure 4.3. It is worth mentioning that the quantity plotted in Figure 4.3 has a factor of $1/p_T$ in it. Weights calculated according to it were multiplied by p_T. Invariant mass spectra for different p_T bins were fitted with a decaying exponential + a Gaussian. The π^0 yield for each p_T bin was extracted using the fit parameters. The efficiency for each p_T bin was calculated as a ratio of a π^0 yield over the number of simulated π^0's going into the detector acceptance, weighted according to the $\frac{h^+ + h^-}{2}$ p_T spectrum. HighTower-1 and HighTower-2 triggers were simulated by requiring a high tower in the event with trigger ADC greater than 8 and 13, respectively.

The effect of simulated efficiency and acceptance corrections applied to the uncorrected π^0 yield is shown in Figure 4.4. Corrected data points are about a factor of 2

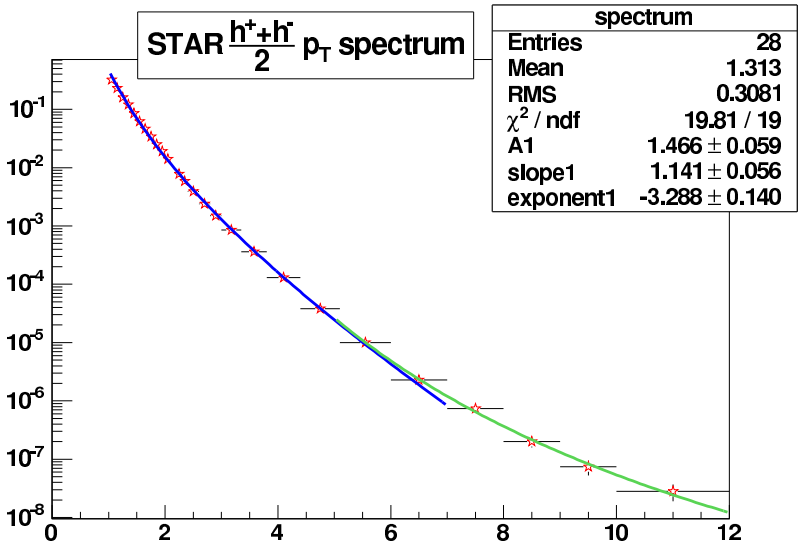

Figure 4.3: Inclusive charged hadron p_T distribution $1/(2\pi p_T)d^2N/dp_T d\eta \mid_{\eta=0}$ for minimum bias collisions. Solid lines are fits to the data points. The data points were fitted with 2 functions of irrelevant nature. For the purpose of scaling the π^0 spectrum it is essential that fit follows the data points closely.

lower than STAR $\frac{h^+ + h^-}{2}$ and PHENIX π^0 spectrum. The source of this discrepancy remains to be understood. This is the work in progress.

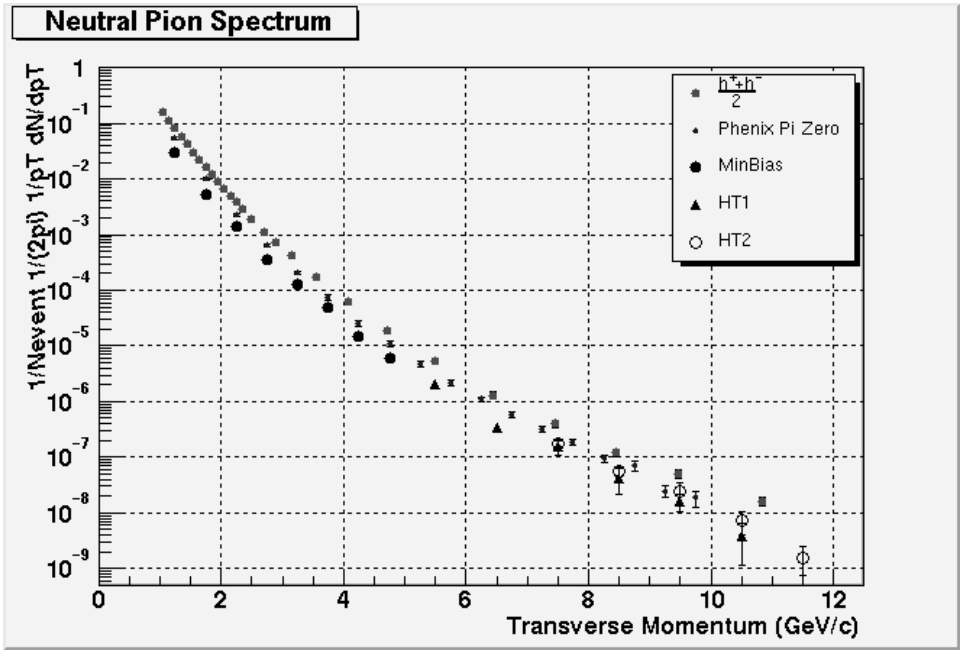

Figure 4.4: Neutral pion yield vs. p_T in dAu with efficiency and acceptance corrections applied (preliminary).

Bibliography

[1] Collins, J.C., Perry, M.J.: Superdense matter: Neutrons or asymptotically free quarks? Phys. Rev. Lett. **34** (1975) 1353

[2] Bourhis, L., Fontannaz, M., Guillet, J.P., Werlen, M.: Next-to-leading order determination of fragmentation functions. Eur. Phys. J. **C19** (2001) 89–98

[3] Group), P.D., Groom, D., et al. Eur. Phys. Journal. **C15** (2000) 1

[4] Owens, J.F., Reya, E., Gluck, M.: Detailed quantum chromodynamic predictions for high p_t processes. Phys. Rev. **D18** (1978) 1501

[5] Adler, S.S., et al.: Absence of suppression in particle production at large transverse momentum in $\sqrt{s_{NN}}$ = 200 gev d + au collisions. Phys. Rev. Lett. **91** (2003) 072303

[6] Adcox, K., et al.: Suppression of hadrons with large transverse momentum in central au + au collisions at $\sqrt{s_{NN}}$ = 130 gev. Physical Review Letters **88** (2002)

[7] Adcox, K., et al.: Centrality dependence of the high-p_t charged hadron suppression in au + au collisions at $\sqrt{s_{NN}}$ = 130 gev. Phys. Lett. **B561** (2003) 82–92

[8] Adler, S.S., et al.: Suppressed π^0 production at large transverse momentum in central au + au collisions at $\sqrt{s_{NN}}$ = 200 gev. Physical Review Letters **91** (2003)

[9] Adler, C., et al.: Centrality dependence of high-p_t hadron suppression in au + au collisions at $\sqrt{s_{NN}}$ = 130 gev. Physical Review Letters **89** (2002)

[10] Gyulassy, M., Plumer, M.: Jet quenching in dense matter. Phys. Lett. **B243** (1990) 432–438

[11] Wang, X.N., Gyulassy, M.: Gluon shadowing and jet quenching in a + a collisions at $\sqrt{s_{NN}} = 200$ gev. Phys. Rev. Lett. **68** (1992) 1480–1483

[12] Thoma, M.H., Gyulassy, M.: Quark damping and energy loss in the high temperature qcd. Nucl. Phys. **B351** (1991) 491–506

[13] Arneodo, M., et al.: Shadowing in deep inelastic muon scattering from nuclear targets. Phys. Lett. **B211** (1988) 493

[14] Adams, J., et al.: Evidence from d + au measurements for final-state suppression of high-p[sub t] hadrons in au + au collisions at rhic. Physical Review Letters **91** (2003)

[15] Antreasyan, D., et al.: Production of hadrons at large transverse momentum in 200-, 300-, and 400-gev pp and $p-$nucleus collisions. Phys. Rev. **D19** (1979) 764

[16] Bland, L.C.: Star results from polarized proton collisions at rhic. (2004)

[17] Bourrely, C., Soffer, J.: Do we understand the single-spin asymmetry for pi0 inclusive production in p p collisions? hep-ph/0311110 (2003)

[18] Letessier, J., Rafelski, J.: Hadrons and Quark-Gluon Plasma. First edn. Cambridge University Press, Cambridge, UK (2002)

[19] Ackermann, K.H., et al.: Star detector overview. Nucl. Instrum. Meth. **A499** (2003) 624–632

[20] Beddo, M., et al.: The star barrel electromagnetic calorimeter. Nucl. Instrum. Meth. **A499** (2003) 725–739